Anal. Chem. **2000,** *72,* 2229−2236

Raman Spectroscopic Imaging Markers for Fatigue-Related Microdamage in Bovine Bone

Jerilyn A. Timlin, Angela Carden, and Michael D. Morris*

Department of Chemistry, University of Michigan, 930 North University Avenue, Ann Arbor, Michigan 48109-1055

Rupak M. Rajachar and David H. Kohn

Department of Biomedical Engineering, University of Michigan, Ann Arbor, Michigan 48109-2125 and Department of Biologic and Materials Sciences, University of Michigan, Ann Arbor, Michigan 48109-1078

Raman spectroscopic markers have been determined for fatigue-related microdamage in bovine bone. Microdamage was induced using a cyclic fatigue loading regime. After loading, the specimens were stained en-bloc with basic fuchsin to facilitate damage visualization and differentiate fatigue-induced damage from cracks generated during subsequent histological sectioning. Bone tissue specimens were examined by light microscopy and hyperspectral near-infrared Raman imaging microscopy. Three regions were defined—tissue with no visible damage, tissue with microcracks, and tissue with diffuse damage. Raman transects, lines of 150−200 Raman spectra, were used for initial tissue surveys. Exploratory factor analysis of the transect Raman spectra has identified spectroscopically distinct chemical microstructures of the bone specimens that correlate with damage. In selected regions of damage, full hyperspectral Raman images were obtained with 1.4-μm spatial resolution. In regions of undamaged tissue, the phosphate ν_1 band is found at 957 cm^{-1}, as expected for the carbonated hydroxyapatic bone mineral. However, in regions of visible microdamage, an additional phosphate ν_1 band is observed at 963 cm^{-1} and interpreted as a more stoichiometric, less carbonated mineral species. Raman imaging confirms the qualitative relationship between the Raman spectral signature of bone mineral and the type of microdamage in bovine bone. Two tentative explanations for the presence of less carbonated phosphate in damaged regions are proposed.

In mammalian bone, small cracks are formed as a result of repetitive mechanical stresses. These fatigue-related microcracks have been observed in vivo in human, canine, bovine, and rat bone. Fatigue-related microcracks, as detected histologically with basic fuchsin staining,[1−3] range in length from 25 to 300 μm. Despite the ability to spatially resolve small-scale damage, the specific microstructural parameters leading to a particular spatial array of damage are unclear. We propose that Raman spectroscopy is sufficiently sensitive to differences in mineral composition that it can be used to identify areas that are damaged or damage-susceptible and possibly explain why certain regions of bone are subject to damage. By identifying and imaging the Raman spectral features characteristic of damaged regions, we can identify the mineral differences associated with damage and develop spectroscopic predictors of fatigue-related bovine bone microdamage.

Bone mineral is primarily a nonstoichiometric, carbonated hydroxyapatite lattice. Carbonate typically substitutes into the lattice for PO_4^{3-} (B-type carbonate). Other common substitutions are HPO_4^{2-}, CO_3^{2-} in place of an OH^- (A-type carbonate), Cl^-, and/or F^-. The degree of substitution and mineralization varies with bone type, bone age, and pathological disease state.[4] In vivo, bone continuously renews and repairs itself in response to changing functional needs through a process called remodeling. However, with age, microdamage may accumulate faster than the bone can repair the damage. The accumulation of microdamage compromises the mechanical integrity of bone and may ultimately contribute to age-related bone degradation and fatigue fracture in cortical and trabecular bone.[5]

Fatigue-related microcracks in bone have been hypothesized to lead to decreases in the mechanical properties of bone, specifically elastic modulus and fracture toughness.[6] However, the details of microstructural fatigue damage mechanisms and their relation to the mechanical properties' degradation remain unknown. Cortical bone can withstand a 10−25% reduction in elastic modulus before an increase in the microcrack burden is detected, suggesting that smaller scale damage mechanisms are important. Laser scanning confocal microscopy has been used to generate three-dimensional images of microdamage in cancellous bone at high spatial resolution.[7] It has been demonstrated that crosshatch and diffuse staining in addition to discrete microcracks are indicative of damage in cortical and trabecular bone. Diffuse matrix damage is characterized by pooled regions of diffuse basic fuchsin staining in which individual microcracks are not readily resolved

* To whom correspondence should be sent: (phone) (734)764-7360; (fax) (734)764-8815; (e-mail) mdmorris@umich.edu.

(1) Frost, H. *Henry Ford Hosp. Bull.* **1960**, *3*, 25−35.
(2) Burr, D.; Stafford, T. *Clin. Orthopaedics Relat. Res.* **1990**, *260*, 305−308.
(3) Burr, D.; Hooser, M. *Bone* **1995**, *17*, 431−433.
(4) Ham, A. W. *Histology*, 9th ed.; J. B. Lippincott Co.: Philadelphia, 1987.
(5) Schaffler, M.; Choi, K.; Milgrom, C. *Bone* **1995**, *17*, 521−525.
(6) Burr, D. B.; Turner, C. H.; Naick, P.; Forwood, M. R.; Ambrosius, W.; Hasan, M. S.; Pidaparti, R. *J. Biomech.* **1998**, *31*, 337−345.
(7) Fazzalari, N. L.; Forwood, M. R.; Manthey, B. A.; Smith, K.; Kolesik, P. *Bone* **1998**, *23*, 373−378.

10.1021/ac9913560 CCC: $19.00
Published on Web 04/12/2000

and is a precursor to well-defined singular microcracks.[8] Recently, Rajachar et al. have implicated diffuse ultrastructural damage development and subsequent microcrack nucleation and growth as the incipient mechanism of fatigue damage.[9] By using acoustic emission and modulus reduction methods, they were able to establish three distinct time points in the fatigue damage process in bone and showed that diffuse damage acted as a plastic zone and was a precursor to formal microcracking.

It is well known that the vibrational spectrum of a material can reflect perturbations in the material's microstructure. Although infrared spectroscopy was the first vibrational spectroscopy used to characterize bone tissue,[10−13] Raman spectroscopy is often simpler to use when examining biological specimens because there is little interference from water and no need for complicated sample preparation. Frozen or embedded specimens with thicknesses ranging from less than 1 μm to that of intact bone can be analyzed with ease. Use of near-infrared excitation eliminates the protein fluorescence that initially hindered observation of the Raman spectrum of whole bone.[14]

In stoichiometric hydroxyapatite, the phosphate ν_1 vibration is found at 963 cm^{-1}. As the mineral becomes less perfect, i.e., the mineral lattice has excessive vacancies and/or substitutions or a decreased crystalline-to-amorphous ratio, this band envelope shifts to lower wavenumbers and broadens. The phosphate ν_1 vibration ($\sim$960 cm^{-1}) and monohydrogen phosphate ν_1 vibration ($\sim$1003 cm^{-1}) have been shown to be a good probes of mineral structure and substitution.[14,15]

Specimens such as bone are complex composite materials. The chemical and physical properties of one very small volume do not accurately represent the specimen as a whole. For this reason, single-point spectroscopy is not sufficient to accurately describe the chemical composition of bone. Instead, the addition of spatial information in either one spatial dimension (a Raman transect) or two spatial dimensions (a Raman spectroscopic image) is needed. Spatial dimensionality enables a powerful diagnostic tool for exploring and characterizing bone microstructure with light microscopy spatial resolution. We have previously employed Raman spectroscopic imaging techniques coupled with multivariate analysis to image the phosphate environments in mature and immature canine trabecular bone.[16] We have also explored the concentric lamellar structure around the cortical bone remodeling unit, the osteon.[15] Using transects, we identified three different phosphate mineral species, a noncarbonated apatite, a carbonated apatite, and an amorphous-like apatite. We mapped the location of these mineral species, nonmineralized osteoid, and the blood vessel wall radially from the center of the osteon.

Our high-resolution image data sets contain thousands of Raman spectra. Multivariate image processing has generated higher contrast images and more chemically informative images from complicated data sets than traditional univariate methods.[17] Techniques such as principal component analysis and factor analysis employ the internal covariance of the large data sets to reduce the data to smaller manageable sets of significant factors.[18,19] Changes in the background are easily distinguished from changes in the Raman spectra. The redundancy of massive image data sets allows the observation of small changes in Raman band shape or position that might otherwise go unnoticed. These changes reflect differences in chemical composition and physical properties that define the chemical contrast. It is the power of factor analysis that allows us to develop Raman imaging as a tool for the characterization of normal and damaged bone microstructure.

EXPERIMENTAL SECTION

Specimen Preparation. Cortical bone specimens were prepared from mature bovine femoral central diaphyseal sections. The specimen sectioning procedure and fatigue loading regime are described in detail elsewhere.[8,9] Briefly, the fatigue loading regime was developed on the basis of the specimens' initial elastic moduli. Notched specimens were loaded parallel to the long axis of the bone, following a sinusoidal waveform, over an effective strain range ($\Delta\epsilon_{eff} = \Delta\sigma/E_0$) of 0−3000 $\mu\epsilon$, at a frequency of 1 Hz. Loads were selected such that the peak strain at the notch root was 3000 $\mu\epsilon$. This maximum strain was chosen such that it was in the upper range of physiologic strain experienced by cortical bone during normal loading.[20]

Specimens were mechanically fatigued in one of three different fatigue loading schemes: control or no loading, fatigue to onset of acoustic emission (AE), or fatigue to 1% elastic modulus reduction (ΔE). With this approach, a temporal sequence of damage progression was established. The validity of AE and ΔE methods in determining the progression of damage in bone has been previously shown.[8,9]

Following fatigue loading, specimens were stained en-bloc using a graded series of 1% basic fuchsin solutions in ethanol.[3] Basic fuchsin is a fluorescent stain that preferentially binds to exposed external and internal defects in biological structures, specifically osteoid in bone. Bulk staining with basic fuchsin prior to histological sectioning enables visualization of microdamage and differentiation between cracking due to mechanical loading and artifactual cracks induced during histological preparation. Each stained specimen was embedded in poly(methyl methacrylate) and serially sectioned (150 μm thick) parallel to the 4.5-mm thickness. Laser-scanning confocal microscopic analysis was employed to quantify the type and spatial distribution of the microdamage and identify regions that were analyzed via Raman spectroscopic imaging.

(8) Rajachar, R. M.; Chow, D. L.; Weissman, N. A.; Curtis, C. E.; Kohn, D. H. In *Acoustic Emission: Standards and Technology Update*; Vahaviolos, S. J., Ed.; ASTM: Philadelphia, 1999; pp 3−21.

(9) Rajachar, R. M.; Chow, D. L.; Kohn, D. H. *J. Biomech.*, in press.

(10) Rey, C.; Shimizu, M.; Collins, B.; Glimcher, M. J. *Calcif. Tissue Int.* **1990**, *46*, 384−394.

(11) Rey, C.; Shimizu, M.; Collins, B.; Glimcher, M. J. *Calcif. Tissue Int.* **1991**, *49*, 383−388.

(12) Pleshko, N. L.; Boskey, A. L.; Mendelsohn, R. *J. Biophys.* **1991**, *60*, 786−795.

(13) Paschalis, E. P.; DiCarlo, E.; Betts, F.; Sherman, P.; Mendelsohn, R.; Boskey, A. L. *Calcif. Tissue Int.* **1996**, *59*, 480−487.

(14) Pezzuti, J. A.; Morris, M. D.; Bonadio, J. F.; Goldstein, S. A. *Biomedical Optics*, San Jose, CA, International Society for Optical Engineering, 1998; pp 270−276.

(15) Timlin, J. A.; Carden, A.; Morris, M. D. *Appl. Spectrosc.* **1999**, *53*, 1429−135.

(16) Timlin, J. A.; Carden, A.; Morris, M. D.; Bonadio, J. F.; Hoffler, C. E., III; Kozloff, K. M.; Goldstein, S. A. *J. Biomed. Opt.* **1999**, *4*, 28−34.

(17) Geladi, P.; Grahn, H. *Mulitvariate Image Analysis*; John Wiley and Sons: Chichester, U.K., 1996.

(18) Drumm, C. A.; Morris, M. D. *Appl. Spectrosc.* **1995**, *49*, 1331−1337.

(19) Shaver, J. M.; Christensen, K. C.; Pezzuti, J. A.; Morris, M. D. *Appl. Spectrosc.* **1998**, *52*, 259−264.

(20) Lanyon, L.; Goodship, A.; Pye, C.; MacFie, J. *J. Biomech.* **1982**, *15*, 141−154.

The Raman spectroscopy and imaging were performed on selected specimens. Initially, the specimens were explored by taking at least six Raman transects per specimen through areas of visible microdamage and areas that appeared normal. Follow-up high-definition images were taken in areas that exhibited spectroscopically different mineral species. Comparisons were made between the spectroscopic properties of damaged areas and those of nondamaged areas, as well as between the spectroscopic properties of the specific damage types—diffuse matrix damage and microcracks.

Raman Spectroscopy and Imaging. Raman transects and images were taken from three morphologically distinct regions of bone tissue—no visible damage, visible microcracks, and diffuse damage. All Raman spectral data were acquired using the hyperspectral Raman line-imaging system described previously.[21] The system consists of a standard fluorescence microscope (Olympus BH-2) used in epi-illumination mode. Raman scatter is projected onto the 25-μm entrance slit of a NIR-optimized axial transmissive spectrograph (f/1.8, Kaiser Optical Systems, Inc.). Dispersed light is collected with a CCD detector and read out to a Pentium-based computer. In the current applications, a 200-mW 785-nm diode laser (SDL, Inc.) was used as the excitation source and a holographic notch filter (Kaiser Optical Systems, Inc.) was employed to reject the Rayleigh scatter.

When acquiring Raman transects, the laser was focused with a 20×/0.75 NA Fluar objective (Carl Zeiss) to a 1.5-μm-diameter spot at the specimen. The power density at the specimen was ~70 mW/μm^2. The line of Raman spectra was generated by scanning the specimen at 2.0-μm intervals in one direction with an X−Y translation stage (New England Affiliated Technologies). Raman scattered light was dispersed onto a thermoelectric cooled CCD (256 × 1024 pixels, Andor Technology) operating at −30 °C. A typical transect contained 200 Raman spectra and was acquired in 30 min or less. Initially, the specimens were explored by taking at least six transects per specimen through areas of visible microdamage and areas that appeared normal. Raman spectra were collected from 400 to 1800 cm^{-1}.

For Raman imaging, a Powell lens line generator was inserted into the illumination optics and the laser was focused with a 20×/0.75 NA Fluar objective (Carl Zeiss). The resulting line was approximately 0.6 μm × 60 μm. The power density was less than 1.0 mW/μm^2. Raman spectra corresponding to each point along the line were projected onto a liquid N_2-cooled CCD (100 × 1340 pixels, Princeton Instruments). The image was constructed by incrementing the X−Y translation stage 0.7 μm between lines of Raman spectra. The increment in the motion direction was selected such that the pixels in the final image would be approximately square. A typical image (100 × 100 pixel definition) was acquired in 8 h or less.

Data Analysis. All data analysis was performed in Matlab 5.2 (Mathworks, Inc) using vendor-supplied and custom-written scripts. Data were preprocessed using a median filter to remove cosmic events, artifactual spikes in the Raman data. Mineral information-rich spectral subregions for multivariate analysis were selected because the factor analysis procedure has been previously shown to be more effective when it is concentrated to a small spectral region.[15] The Raman shift frequency and wavelength-dependent instrument response was calibrated using a Hololab calibration accessory. (Kaiser Optical Systems, Inc.) All of the calibrations were verified against the Raman spectrum of Teflon obtained before and after image acquisition.

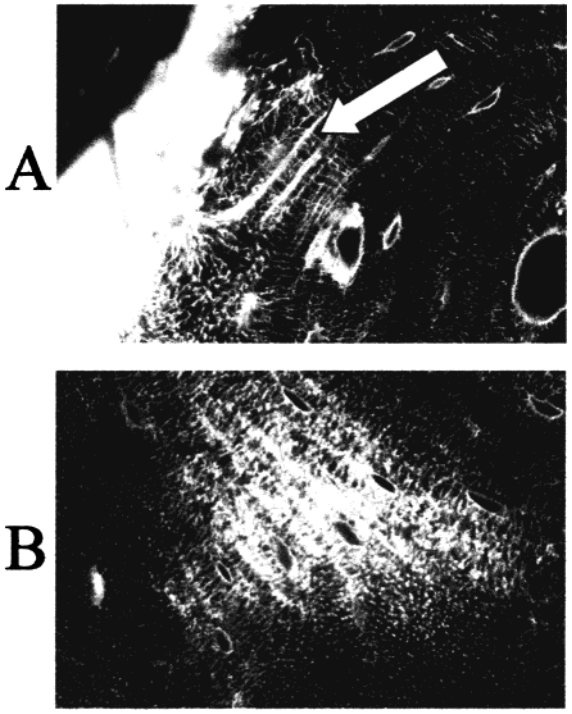

Figure 1. Laser-scanning confocal microscope images of two types of microdamage, 60× (oil). (A) White arrow indicates two microcracks, approximately 30−50 μm in length; (B) stained central area indicates tissue with diffuse damage.

Exploratory principal-component-based factor analysis was performed to reduce the large image data sets to a few significant component factors. The factors were rotated to impart physical meaning using nonnegativity and second-derivative constraints known to be valid for Raman spectra. The development of the principal component and factor analysis techniques for the analysis of Raman spectra has been discussed previously.[18,19] Details of the specific application to Raman spectroscopic imaging of the chemical species within bone are presented elsewhere.[16]

RESULTS AND DISCUSSION

While microdamage does occur in vivo, additional microcracks and diffuse damage can be induced and extended by cyclic fatigue loading in vitro. Under the laser-scanning confocal microscope, it was observed that localized fatigue loaded regions of bone tissue either showed no signs of visible damage or had one of two types of visible damage, diffuse matrix damage, or visible microcracks. (Figure 1) In Figure 1A, the white arrow points to two microcracks running diagonally through the center of the image. The cracks are approximately 30−50 μm in length. Figure 1B shows a diffuse damage area. Diffuse matrix damage is characterized by pooled regions of basic fuchsin staining where individual microcracks are not readily resolved and is a precursor to well-defined singular microcracks.[8] The diffuse damage is the white circular area in the center of the image.

Raman Transects. To confirm that the basic fuchsin staining procedure used to visualize microcracks does not alter the Raman

(21) Christensen, K. C.; Morris, M. D. *Appl. Spectrosc.* **1998**, *52*.

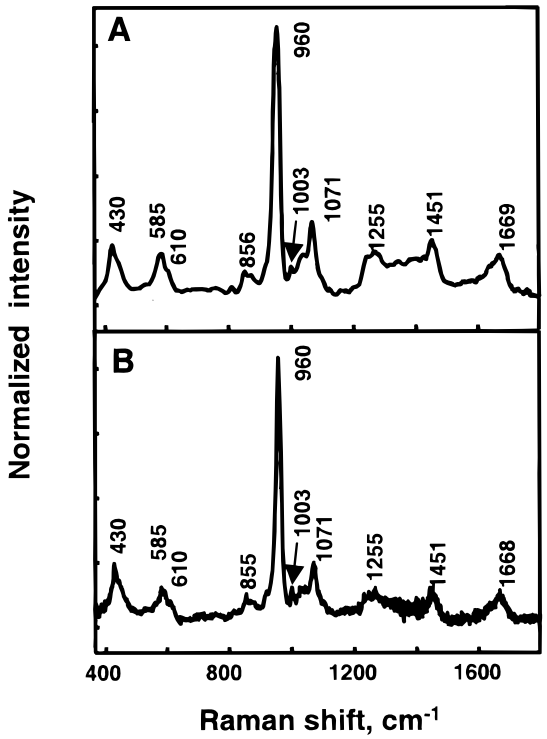

Figure 2. (A) Raman spectrum of whole, unfixed bovine bone. (B) Raman spectrum of basic fuchsin stained bovine bone mounted on glass microscope slide. The glass background has been subtracted. Both spectra have been corrected for instrument response and have been normalized to phosphate $\nu_1 = 1$.

spectrum of bovine bone, several Raman spectra of these basic fuchsin-stained bovine specimens were compared to a Raman spectrum obtained from a specimen that had not undergone any staining or fixing procedures. No significant differences were observed. Panels A and B of Figure 2 show the Raman spectra of whole unfixed bovine bone and basic fuchsin stained bovine bone, respectively.

The bands assigned to vibrations of carbonated calcium phosphate in an apatitic lattice are 430 and 451 (phosphate ν_2); 585, 590, and 610 (phosphate ν_4); 960 (phosphate ν_1); 1003 (monohydrogen phosphate ν_4); 1030 and 1045 (phosphate ν_3); and 1071 cm^{-1} (B-type carbonate ν_3). Protein vibrations are responsible for the remaining bands—1250 (amide III); 1451 (CH_2 bending/deformation), and 1668 cm^{-1} (amide I). These assignments are in good agreement with those given previously in the literature.[22,23] Although the vibration envelope at ~855−870 cm^{-1} remains controversial, the 855- and 871-cm^{-1} vibrations observed are most likely due to the C−C stretch of proline and hydroxyproline, respectively.[24]

Each Raman transect data set was analyzed individually using the factor analysis procedures developed previously.[19] In this study, the analysis was confined to the Raman scattering region between 800 and 1180 cm^{-1}. This region is rich in Raman spectral signatures from the mineral component of bone, including the common substitutions such as carbonate and monohydrogen phosphate. By limiting the spectral region to a smaller subset, the contributions from background shifts and protein components are minimized allowing the factor analysis to focus specifically on the mineral components of bone.

After analyzing the Raman transects, a pattern became evident. Whenever a transect included spectra from an area near visible microdamage, microcrack or diffuse, at least one additional significant factor was present. These additional factors all had signal in the phosphate ν_1 region, giving those data sets two phosphate species components, ~957 cm^{-1} and ~963 cm^{-1}. For example, Figure 3 shows the recovered mineral factors (A−C) and scores (D−F) from one of the Raman transect data sets. This

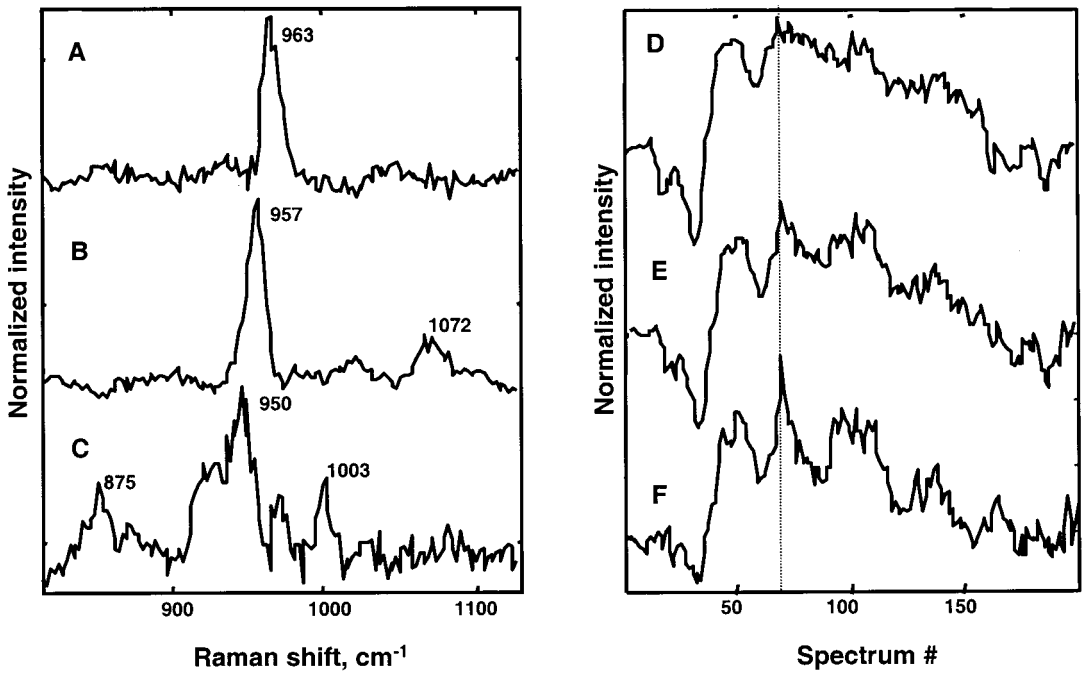

Figure 3. Phosphate factors and scores from Raman transect data. Factors and scores have been normalized so that the highest intensity in each one is equal to 1.0. (A, D) Noncarbonated hydroxyapatite factor and corresponding score; (B, E) B-type carbonated hydroxyapatite factor and corresponding score; (C, F) poorly mineralized osteoid from bone-forming cells and corresponding score. The dashed line indicates spectrum 75.

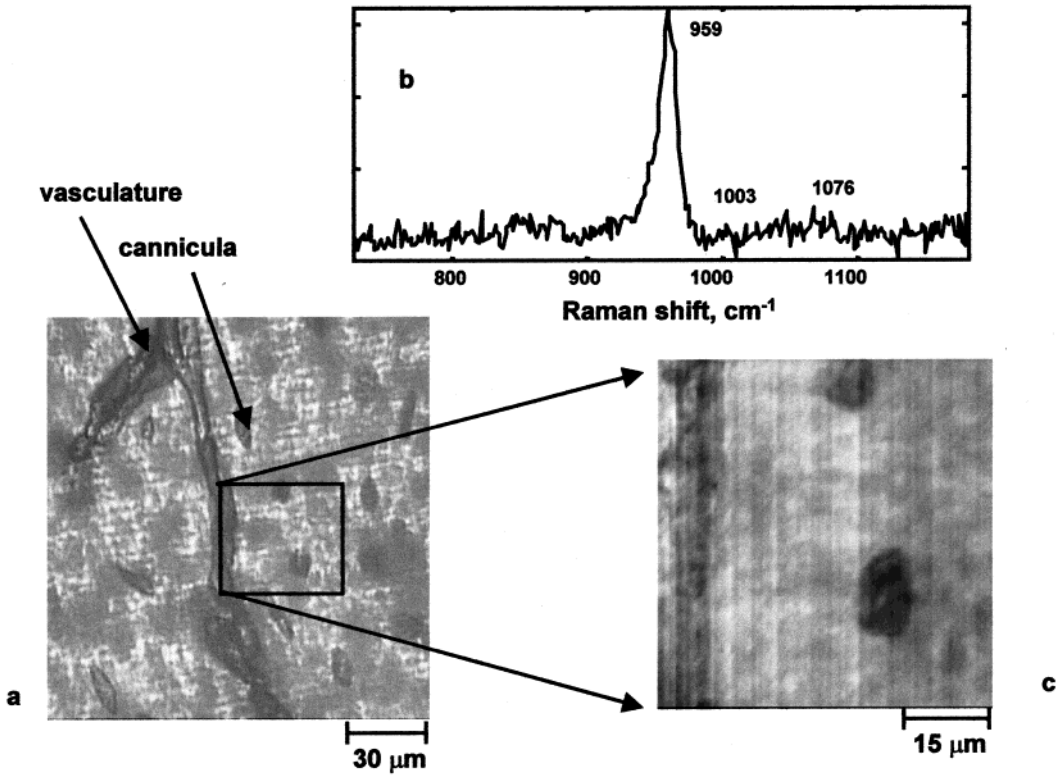

Figure 4. Raman imaging results from area with no visible damage. (a) Transmission bright-field image of basic fuchsin-stained bone specimen. (b) Single recovered factor representing the Raman spectrum of bone mineral. (c) Score image of carbonated apatite distribution in nondamaged bone. Score image is 63 μm $\times$ 60 μm with 1.4-μm spatial resolution.

transect contained 200 spectra taken at 2.0-μm intervals extending outward from a microcrack ~170 μm in length. Each factor and score has been normalized for display purposes so that the highest intensity within that factor or score is equal to 1.0.

Factors represent the Raman spectra of spatially varying components within the data set. The factor shown in Figure 3A represents a near-stoichiometric hydroxyapatite component. The phosphate ν_1 band is positioned at 963 cm^{-1} and the B-type carbonate substitution band at 1072 cm^{-1} is missing. Factor 3B represents the typical carbonated hydroxyapatite Raman signal. The phosphate ν_1 band is at 957 cm^{-1} and is broad and asymmetric. There is a strong band at 1072 cm^{-1} indicating a substantial amount of B-type carbonate substitution in this phosphate mineral. Factor 3C represents poorly mineralized bone tissue component. The phosphate ν_1 band is weak and shifted to a much lower 950 cm^{-1}. This band position indicates the mineral more closely resembles amorphous calcium phosphate rather than calcium phosphate in an apatitic lattice. Also, there is a strong monohydrogen phosphate band at 1003 cm^{-1}. While monohydrogen phosphate can be incorporated into the mineral lattice of bone, it is also present in high concentrations in the bone-forming cells commonly found in nonmineralized osteoidal tissue. We have found signal of this type to be indicative of areas where active remodeling was occurring.[16]

A score indicates where that particular factor/component is located along the transect. Since the transects sampled a distance of 400 μm very coarsely (2 μm between each spectrum) and bone is very inhomogeneous, the factor scores are not easily interpreted. In addition to important Raman spectrum variations, they also reflect small sample surface variations and boundaries such vasculature and lacunae. For example, score 3F shows that the transect most likely passed through a lucuna, the structure that houses bone cells high in monohydrogen phosphate. At approximately spectrum 75, marked by the vertical dashed line, the score 3F rises sharply—indicating that a higher concentration of component 3C (nonmineralized osteoid) was found at this point. Score 3D does not show a maximum at spectrum 75 and spectrum 75 of score 3E is of much lower intensity than that of 3F. This is because lacunae are not well mineralized.

Raman Imaging of Bone with No Visible Damage. To verify our initial observations of an additional mineral component associated with microdamaged bone, we acquired at least three high-definition Raman line images through each of the following areas—no visible damage, visible microcracks, and diffuse damage. In all cases, we found no evidence of abnormal (noncarbonated) bone mineral in the areas of no visible microdamage.

Figure 4a shows a transmission bright-field image of a bovine bone specimen. There is no visible damage in this area, only normal bone tissue and vasculature. It is likely that the large blood vessels are no longer intact after sample preparation and that the basic fuchsin stain simply pools in the canals. We chose to take a high-definition Raman image of the 63 μm $\times$ 60 μm region designated by the square. Panels b and c of Figure 4 contain the results of multivariate factor analysis on the 9000 spectra Raman image data set.

The data were preprocessed by filtering out the cosmic events and correcting for wavelength-dependent instrument response. The spectral range was truncated to approximately 750−1180 cm^{-1} to direct the factor analysis toward the changes in the mineral component bands. A visual inspection of the principal components

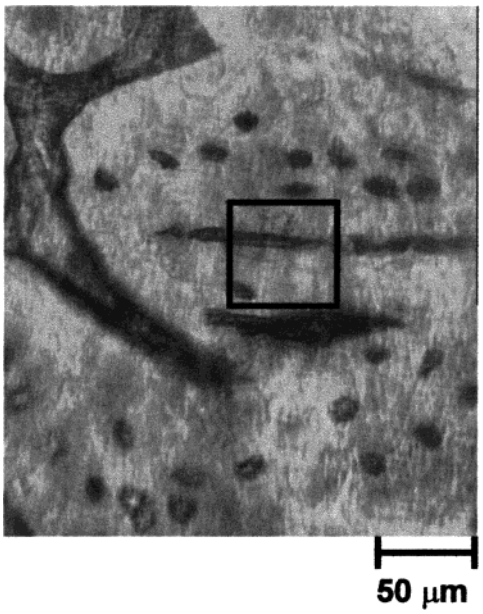

Figure 5. Bright-field transmission image of bovine bone with visible microdamage. Microcrack is slightly above and to the right of center. Crack length is ~120 μm. A black square indicates the region corresponding to the Raman image.

indicated that only four eigenvectors needed to be retained for rotation. After rotation, three of the four components contained only background signal and are not shown. The other factor, representing Raman signal from the bone mineral, is shown in Figure 4b.

The phosphate ν_1 band is at 959 cm^{-1}, characteristic of carbonated calcium phosphate in an apatitic lattice. Raman image contrast is obtained by calculating the score image of this factor. (Figure 4c) The small inhomogeneities in the bone tissue are easily visible at the 1.4-μm resolution. As expected, the blood vessel and canaliculi show no mineral content. It should be noted when comparing the bright-field transmission image to the Raman image that the diagonal lines in the bright-field image are striations in the polymer mounting media caused by the cutting procedure. They do not appear in the Raman image due to of the confocality of our imaging system.

Raman Imaging of Bone with Visible Microdamage. Figure 5 shows a bright-field transmission image of a bovine bone with visible microdamage. The microcrack (approximate length 120 μm) is slightly above and to the right of the center. A 9800-pixel high-definition Raman image was acquired through the microcrack. The area corresponding to the Raman image is outlined by the black square.

The results of multivariate factor analysis on a Raman data set through a microcrack are shown in Figure 6. After the initial eigenanalysis, six eigenvectors were retained for further rotation into factors. Three of the factors were background features and a fourth was a weak protein signature. The protein has a weak signature not necessarily because there is little protein but because there are not any strong protein bands in the spectral subregion analyzed. The score image corresponding to the protein factor showed the protein was located in the lacuna in the lower left-hand corner of the image.

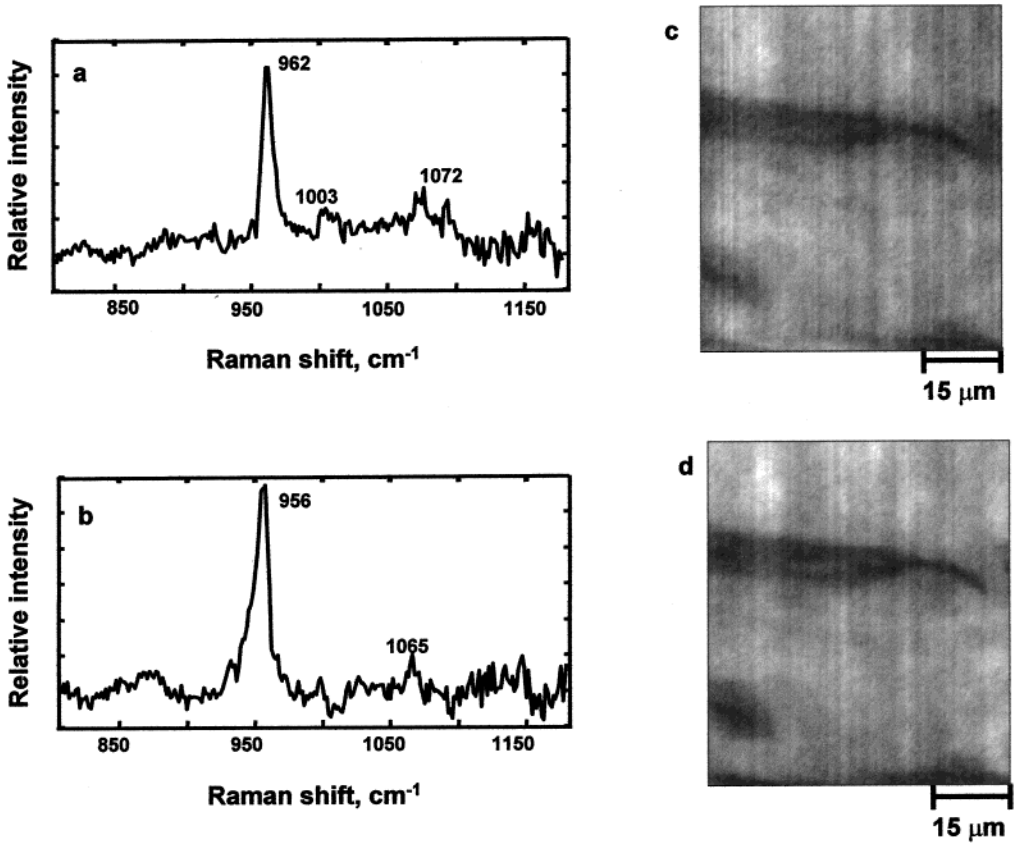

Figure 6. Raman imaging results from area of visible microcrack. (a, c) More stoichiometric apatite factor and corresponding score image; (b, d) normal carbonated apatite in bone and corresponding score. Score images are 52 μm × 60 μm with 1.4-μm spatial resolution.

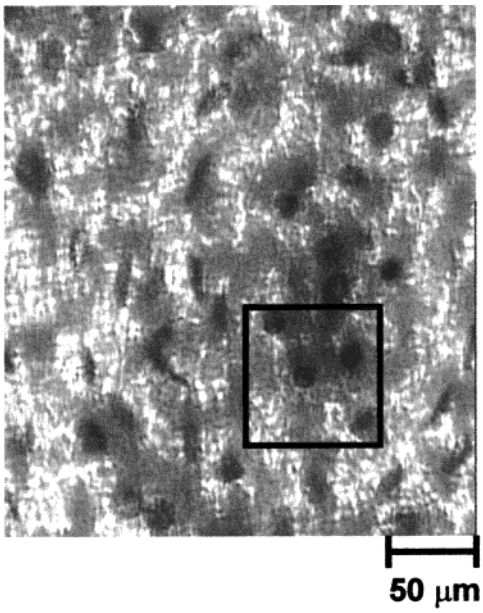

Figure 7. Bright-field transmission image of bovine bone with possible diffuse microdamage. The damage region is dark because of uptake of basic fuchsin stain. The black square indicates the region corresponding to the Raman image and is chosen to include mostly diffuse damaged tissue.

The remaining two factors represented mineral Raman spectra and are shown in Figure 6a and b. As in the transect data, an additional factor with the phosphate ν_1 at a significantly higher wavenumber position than that of the normal carbonated apatite of bone (963 vs 956 cm^{-1}) was observed. The 956-cm^{-1} band in factor 6b is also asymmetric. It is broader on the left side (lower wavenumbers), possibly due to the presence of additional substituted or amorphous-like apatite species. The score images (Figure 6c and d) map the spatial locations of these two phosphate species factors. Differences in score images 6c and 6d are seen in the left center and right center areas, as well as the upper right corner, near the crack tip. It is unclear whether this different mineral signature is a cause or effect of the microdamage.

Raman Imaging of Bone with Diffuse Damage. Figure 7 shows a bright-field transmission image of the area of diffuse damage. The highlighted black rectangle indicates the area of the Raman image. After eigenanalysis of the 9800 spectra data set, five eigenvectors had significant Raman signal rather than noise and were retained for rotation. Completing the rotation resulted in three background and two mineral factors. The background factors are similar to those in the microcrack image data and are not shown. The mineral factors are shown in panels a and b of Figure 8, while the corresponding score images are shown in Figure 8c and d, respectively. Factor 8a contains all of the bands that comprise normal bone tissue Raman spectra, but the phosphate ν_1 (961 cm^{-1}) is slightly higher than the expected value of 959−960 cm^{-1}. However, it is not quite as high as the additional phosphate species seen at 963 cm^{-1} in the image through a microcrack region. Factor 8b has some signal in the phosphate ν_1 envelope but not very much. Score image 8d confirms that this factor is mostly noise. Diffuse damage is a smaller scale damage

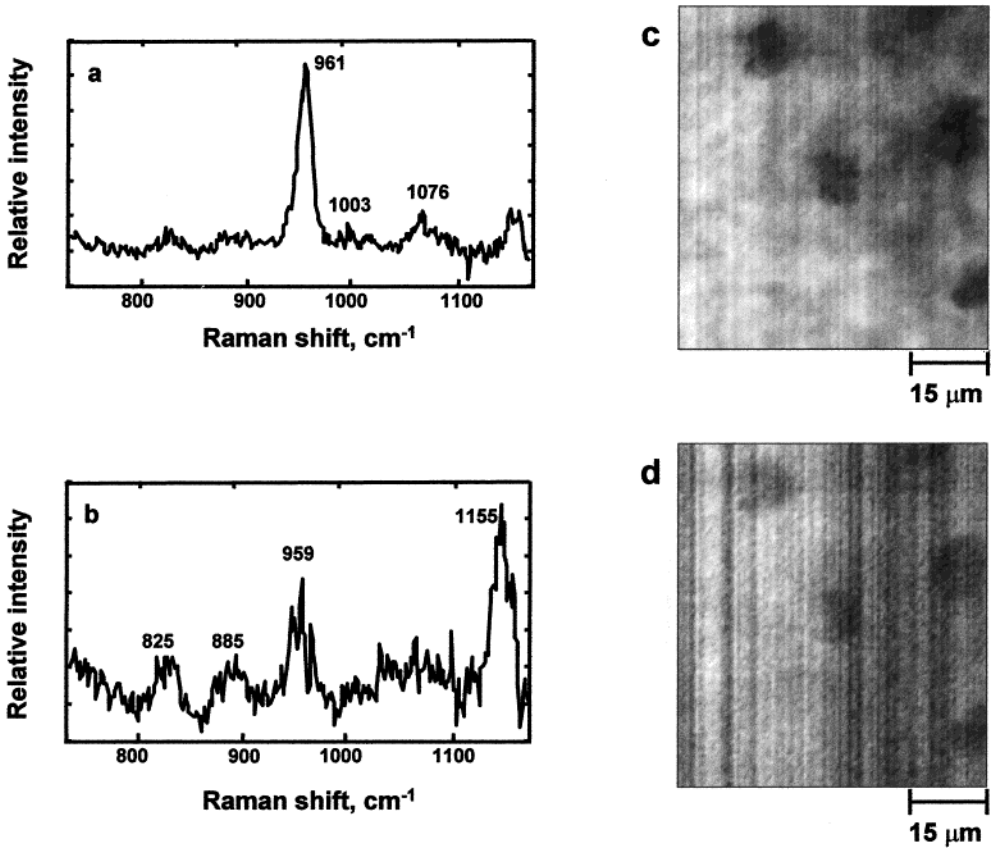

Figure 8. Raman imaging results from diffuse damage region. (a, c) Slightly more stoichiometric apatite factor than normal bone and corresponding score image; (b, d) weakly contributing mineral species and corresponding score. Score images are 63 μm × 70 μm with 1.4-μm spatial resolution.

mechanism than microcracking and therefore is associated with more subtle chemical changes as evidenced in the Raman spectral images. The vertical stripes visible in that image are artifacts from slight imperfections in our slit. They are more pronounced in very noisy images.

Physical Interpretation of Changes in Raman Data and Impact of Results. We attribute the different phosphate ν_1 spectral components in damaged bone to the presence of different mineral species. It is possible that the phosphate ν_1 band could shift in response to residual strain on the mineral lattice, particularly at the crack tip. At the pressures to which these specimens were subjected, the observed shifts should be less than 1 cm^{-1} instead of the 4−6-cm^{-1} shifts that we observe.[25] It is more likely that the different spectral components arise from phosphate in different local environments.

There are two possible alternative explanations for our observations of different phosphate species in our Raman images. (1) The presence of a more stoichiometric mineral alters the structural stability of the bone and therefore damage is more likely to propagate through this region. (2) The energy generated from the propagation of a crack causes the mineral to undergo a phase transformation and/or amorphization as is commonly seen in geological minerals and synthetic apatites.[26] At the present time, the former hypothesis is considered less likely since multiple phosphate bands were not observed in any of the undamaged sections we analyzed. While we do not yet know with certainty whether the abnormal mineral present in microdamaged bovine bone is a cause or an effect of the damage, we can assert that anything, including aging or disease, that causes mineral crystallite size, amorphous-to-crystalline ratio, or amount of carbonation to change, may increase damage susceptibility.

(22) Wuthier, R. E. *Connect. Tissue Res.* **1989**, *22*, 27−33.
(23) Penel, G.; Leroy, G.; Bres, E. *Appl. Spectrosc.* **1998**, *52*, 312−313.
(24) Kirchner, M. T.; Edwards, H. G. M.; Lucy, D.; Pollard, A. M. *J. Raman Spectrosc.* **1997**, *28*, 171−178.
(25) Xu, J.; Gilson, D. F. R.; Butler, I. S.; Stangel, I. *J. Biomed. Mater. Res.* **1996**, *30*.
(26) Vaidya, S. N.; Karunakaran, C.; Pande, B. M.; Gupta, N. M.; Iyer, R. K.; Karweer, S. B. *J. Mater. Sci.* **1997**, *32*, 3213−3217.

CONCLUSIONS

We have demonstrated the power of Raman microspectroscopy and imaging for exploring the heterogeneous chemical microstructure of bone. The high-definition Raman imaging system combined with multivariate data analysis allows subtle differences in mineral composition to be observed in fatigued bovine bone. We have identified spectral markers in the phosphate ν_1 spectral region for different phosphate species within bovine microdamaged bone. These phosphate species correlate with the presence of visible microcracks. While Raman spectral shifts are routinely used to characterize physical properties such as elastic modulus and hardness of polymers and semiconductors, this is the first demonstration that similar correlations may be obtainable in bone.

ACKNOWLEDGMENT

The authors thank the following for their financial support: National Institutes of Health through Grant R01-GM53766 (M.D.M.) and training grant NIDCR DE07057 (R.M.R.), the American Chemical Society through the ACS Analytical Division fellowship sponsored by Proctor & Gamble Co. (J.A.T.), the Cellular Biotechnology Training Program through Grant T32-GM08353 (A.C.), the University of Michigan Center for Biomedical Engineering Research, the National Science Foundation through Grant BES 94-10303 (D.H.K.), and the Whitaker Foundation (D.H.K.).

Received for review November 24, 1999. Accepted February 25, 2000.

AC9913560